PHOTONICS Research

All-in-one photoelectric logic gates by Dember photodetectors

Guoyang Cao,[1,2] Changlei Wang,[1,2] Yu Luo,[3] and Xiaofeng Li[1,2,*]

[1]School of Optoelectronic Science and Engineering & Collaborative Innovation Center of Suzhou Nano Science and Technology, Soochow University, Suzhou 215006, China
[2]Key Laboratory of Advanced Optical Manufacturing Technologies of Jiangsu Province & Key Laboratory of Modern Optical Technologies of the Ministry of Education, Soochow University, Suzhou 215006, China
[3]School of Electrical and Electronic Engineering, Nanyang Technological University, Singapore 639798, Singapore
*Corresponding author: xfli@suda.edu.cn

Received 10 February 2023; revised 16 April 2023; accepted 2 May 2023; posted 2 May 2023 (Doc. ID 487509); published 12 June 2023

Photoelectric logic gates (PELGs) are the key component in integrated electronics due to their abilities of signal conversion and logic operations. However, traditional PELGs with fixed architectures can realize only very limited logic functions with relatively low on–off ratios. We present a self-driving polarized photodetector driven by the Dember effect, which yields ambipolar photocurrents through photonic modulation by a nested grating. The ambipolar response is realized by exciting the whispering-gallery mode and localized surface plasmon resonances, which leads to reverse spatial carrier generation and therefore the contrary photocurrent assisted by the Dember effect. We further design a full-functional PELG, which enables all five basic logic functions ("AND", "OR", "NOT", "NAND", and "NOR") simultaneously in a single device by using one source and one photodetector only. Such an all-in-one PELG exhibits a strong robustness against structure size, incident wavelength, light power, and half-wave plate modulation, paving a way to the realization of ultracompact high-performance PELGs.

https://doi.org/10.1364/PRJ.487509

1. INTRODUCTION

With the rapid development of nanophotonic technologies, light has been widely used as the information carrier. Despite the higher data transmission speed of light, terminals such as mobile phones and computers, still use electrons for computing or/and storage. In all these devices, photodetectors (PDs) are used only to convert the optical signal into electricity, but seldom to perform logic operations. Photoelectric logic gates (PELGs) that can realize both signal conversion and logical operation/processing are highly desired in many applications, because they are more conducive and have the advantages of a more compact device integration, lower power consumption, and higher computing speed, as compared with electronic ones. Therefore, PELGs have recently attracted extensive attention in photoelectric devices [1–5].

The PELGs reported thus far can be generally categorized into three types. In the first type, PDs are usually connected in series or parallel to achieve a certain logical function. For example, Bie *et al.* realized the AND function with an on–off ratio of <26 dB by connecting a ZnO/GaN p–n junction ultraviolet (UV) PD with a CdSe nanowire PD in series [6]. Wang *et al.* connected two Schottky-typed UV GaN nanowire PDs in series (parallel) to realize the AND (OR) function [7]. Kim *et al.* constructed a phototransistor based on quantum dots and ZnO bilayer film, and realized the NOT, NOR, and NAND functions with an on–off ratio of 60 dB through series or parallel connections [8]. In the second type, logic functions are realized by the linear superposition of the photocurrents of the PD under different irradiations. For example, Li *et al.* constructed a $CuInS_2/TiO_2$ heterojunction PD and realized the OR function by the linear superposition of photocurrents under UV and visible light irradiations [9]. In the third type, positive and negative photoconductance effects are combined to realize different logical functions. For example, Ding *et al.* connected a SnO_2-based positive photoconductance detector with a SnO_2/graphene-based negative photoconductance detector through different architectures, realizing AND, OR, and NOT functions [10]. However, these PELGs are still confronted with many challenges. For example, the logic functions that can be realized by a single photoelectric device are usually incomplete, or more specifically, most previous designs can realize only one or two logic functions. The realization of an all-in-one device equipped with all five logic operations (i.e., AND, OR, NOT, NAND, and NOR) remains elusive. Furthermore, the on–off ratio is generally low, which cannot be applied to scenarios requiring ultrahigh precision.

Here, we study the so-called all-in-one PELG composed of a single light source and a single PD, which can realize all five

basic logic functions simultaneously. The proposed device makes use of the ambipolar self-driving polarized PD (ASPPD) driven by the Dember effect. In this ASPPD, current ambipolarity is realized through precise manipulation of the photonic responses, i.e., by exciting whispering-gallery mode (WGM) and localized surface plasmon (LSP) resonances, which exhibit reverse spatial distributions; the switching between different logic functions is implemented by configuring the optical system of such PELGs. We also demonstrate that the designed PELG shows a strong robustness against a variety of structure and light source configurations. This study provides a possibility to implement all five basic logic gates based on only one light source and one PD.

2. RESULTS AND DISCUSSION

To realize a full-functional PELG based on one light source and one PD, we construct a self-driving polarized PD with ambipolar current response as shown in Fig. 1. The nested grating is composed of a silver (Ag) square nanowire, $CH_3NH_3PbI_3$ perovskite ($MAPbI_3$) layer, and indium tin oxide (ITO) cladding. A linearly polarized plane wave light is irradiated vertically onto the grating. The angle between the electric field vector ($\vec{E}$) and nanowire axis is defined as the polarization angle with $\theta = 0°$ and 90° for transverse electric (TE) and magnetic (TM) incidences, respectively. The core idea to achieve the ambipolar photocurrent is as follows. On one hand, benefiting from advanced photonic manipulation, the optical field and photogenerated carriers can be controlled to be distributed mainly on the outer (inner) side of the $MAPbI_3$ layer under TE (TM) incidence. This can realize the spatially inversed carrier concentrations under two different polarizations. On the other hand, the Dember effect is taken as the underlying photoelectric response mechanism by which the current direction is determined by the carrier concentration profiles due to the difference in electron and hole mobilities [11]. Such a combination is expected to make the photocurrents of the polarized PD have the so-called ambipolar responses under TE and TM incidences.

We then numerically evaluate the device performance through an accurate optoelectronic simulation. Based on the finite-element method (FEM), the distributions of optical fields and electromagnetic losses within the devices are obtained by solving Maxwell's equations; the distribution, transport, recombination, and collection of carriers are modeled by employing semiconductor continuity and Poisson's equations. Details of the simulation methods [12–16] and parameters of the materials [17–23] are found in our previous publications. It should be noted that we define the positive current as the direction from ITO to $MAPbI_3$. Because the nanowire length is much longer than its lateral sizes, a 2D simulation with only one unit of the grating is used.

Figures 2(a) and 2(b) show the dependences of the photocurrent densities (J) on d_{MAPbI3} and d_{Ag}, where the wavelength $\lambda = 500$ nm and incident power $P = 10$ W/m^2. Here, the bias voltage V_d, d_{ITO}, and W are fixed at 0 V, 80 nm, and 750 nm, respectively, unless otherwise specified. It can be seen that the J values within the considered ranges, i.e., 20 nm $< d_{Ag} <$ 110 nm and 70 nm $< d_{MAPbI3} <$ 110 nm, are almost negative for TE incidence, but positive for TM, displaying an obvious ambipolarity character within a wide range of system configurations. Taking the polarity of the response current rather than the commonly used amplitude as the detection parameter is very beneficial to judge logically "true" or "false." Moreover, the strong robustness in device size facilitates the fabrication of the device.

Further, we explore the ambipolar mechanisms from the microscopy perspective. Here, we choose the system with $d_{Ag} = 55$ nm and $d_{MAPbI3} = 94$ nm, with which $J = -14.1$ (14.1) mA/cm^2 under TE (TM) incidence with an anisotropy ratio of current density $J_{TM}/J_{TE} = -1$. Unless otherwise specified, this configuration is employed in the following sections of this study. Figure 2(c) shows the J spectra of

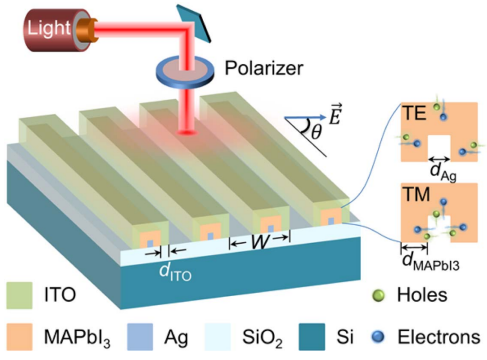

Fig. 1. Scheme diagram of the ASPPD, where d_{ITO}, d_{MAPbI3}, d_{Ag}, W, and θ are the thicknesses of ITO and $MAPbI_3$ layers, side length of Ag, period of the grating, and polarization angle, respectively.

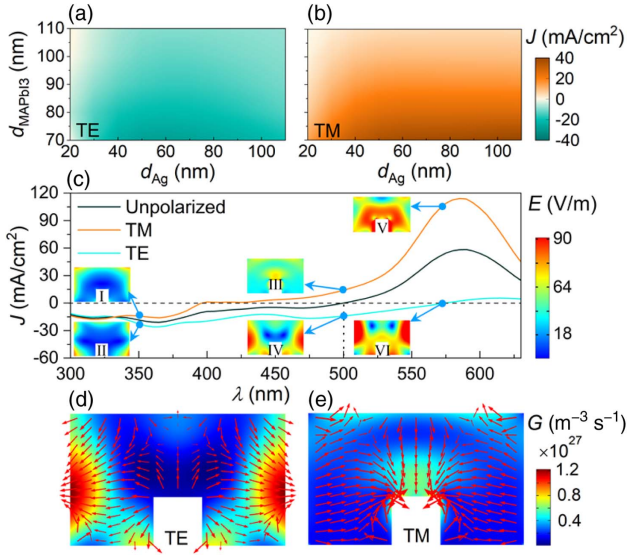

Fig. 2. (a), (b) J of the photodetector versus d_{MAPbI3} and d_{Ag} under TE and TM incidences with $\lambda = 500$ nm, $P = 10$ W/m^2, and $V_d = 0$ V. (c) Spectral responses of the device with $d_{MAPbI3} = 94$ nm and $d_{Ag} = 55$ nm for TE, TM, and unpolarized incidences. Insets (I–VI): distributions of E for λ of 350, 500, and 570 nm. (d), (e) Distributions of G and the vectorial current density (red arrows) in the $MAPbI_3$ layer under TE and TM incidences with $\lambda = 500$ nm. Note that the lengths of the red arrows are taken as logarithm for the convenience of observation.

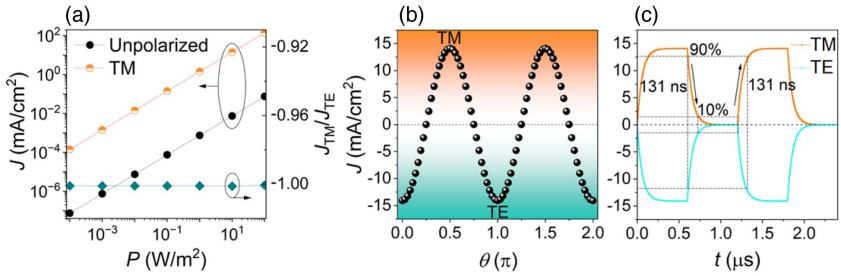

Fig. 3. (a) J and J_{TM}/J_{TE} versus P under TM and unpolarized incidences. (b) J versus polarization angle θ and (c) temporal response of the device, where both TE and TM incidences are included.

the device under TE, TM, and unpolarized incidences. It can be seen that the ambipolar photocurrents under TE and TM incidences can be well maintained in the waveband of 400 nm $\leq \lambda \leq$ 570 nm, indicating strong robustness versus wavelength. Here, we give a brief discussion on the response mechanisms responsible for the photocurrent ambipolarity. Taking $\lambda = 500$ nm as an example, the electric field (E) distributions are illustrated by insets III and IV of Fig. 2(c), which indicate that TE incidence leads to E spatially localized around the outer side of the $MAPbI_3$ layer due to the excitation of WGM resonance. WGM resonance is formed by light propagation along the boundary of an annular cavity or quasi-annular cavity (such as triangle, quadrangle, hexagon), and the resonance peaks are mainly distributed at the cavity boundary [13,24–29]. TM incidence excites LSP resonance, leading to E confined at the inner side of the $MAPbI_3$ layer. According to the LSP resonance theory, when the size of the Ag nanostructure is much smaller than the wavelength of incident visible light, the LSP resonance is easily excited, so that the light field is localized at the interface between the metal nanostructure and the medium, which has been reported widely [30–33].

Accordingly, Figs. 2(d) and 2(e) illustrate the spatial distributions of the carrier generation rates (G) in the $MAPbI_3$ layer under TE and TM incidences, where the red arrows represent the vectorial current densities. It is found that the distributions of G are consistent with that of E, which is reasonable. Under TE incidence, electrons and holes driven by the concentration gradient diffuse to the inner side of the $MAPbI_3$ layer. According to the Dember effect, since electron mobility (12.5 $cm^2\ V^{-1}\ s^{-1}$) is much larger than that of the hole (7.5 $cm^2\ V^{-1}\ s^{-1}$) for $MAPbI_3$ material, an outward photocurrent is formed, as shown by the vectorial current densities. Similarly, under TM incidence, the inward photocurrent is eventually formed.

Obviously, the excitations of the WGM and LSP resonances can be readily modulated by spectral means. For TM incidence with a short λ (e.g., 350 nm), the LSP resonance is absent, and light is mostly absorbed by the outer part of the $MAPbI_3$ layer [see inset I in Fig. 2(c)], leading to a net negative J. Increasing λ from 500 to 570 nm, the LSP resonance is excited and strengthened gradually (see insets III and V), resulting in net positive and increased J values. For TE incidence, when λ is close to 570 nm, WGM resonance is weakened, and there is an obvious enhancement of the optical field in the inner side of the $MAPbI_3$ layer, leading to positive J when $\lambda > 570$ nm. Thus, the ambipolarity modulated by light polarization shows a good spectrum selectivity. In addition, J is negative (positive) when $\lambda <$ (>)500 nm under unpolarized incidence, indicating that ambipolarity can also be achieved by modulating the spectrum. The ambipolarity modulated by the spectrum is also expected to be used to achieve multi-functional logic gates; however, two light sources with modulated powers are required. When the incident power fluctuates, the polarity of the output current may change, resulting in the failure of the logic function. Here, we prefer to achieve these functionalities utilizing the ambipolarity modulated by polarization.

The unpolarized spectral response shown in Fig. 2(c) demonstrates that the J value tends to be zero when $\lambda = 500$ nm. Figure 3(a) compares the J responses under TM and unpolarized incidences. It can be seen that the J values under TM incidence are three orders of magnitude higher than in the unpolarized case, revealing that the polarized PDs proposed here can refrain from the interference of background light (which is always unpolarized) when they are used for logical operation. J versus the polarization angle θ is shown in Fig. 3(b), where a cosine relationship with a period of π can be clearly seen, yielding a peaked positive (negative) J at TM (TE) incidence. Such ease of modulation via light polarization provides a great opportunity to regulate the logical operations. In addition, the temporal response that determines the operation bandwidth is then investigated as shown in Fig. 3(c). The response time of the Dember PD is contributed from three parts, i.e., diffusion time, resistance–capacitance (RC) time, and response time caused by carrier lifetime (τ_t), in which the dominant factor of the whole response time is determined by τ_t as shown in our previous paper [13]. Figure 3(c) shows that τ_t of such a device is 131 ns, which is much shorter than previous reports [3,5–9], indicating a high operation bandwidth of the polarized PD.

Finally, we utilize the ASPPD to construct a full-functional PELG as shown in Fig. 4(a). The working principle is explained as follows. The laser emits a beam of linearly polarized light with $\lambda = 500$ nm, which passes through the first polarization beam splitter (PBS_1) to lock the polarization direction. The polarization direction of the parallel vibration component locked by PBS_1 is regulated through the half-wave plate (HWP). The beam is then decomposed into a parallel vibration component (i.e., TM wave) and vertical component (i.e., TE wave) by PBS_2. The two beams are decomposed into four beams by two 50%:50% beam splitters (BS_1 and BS_2), which are, respectively,

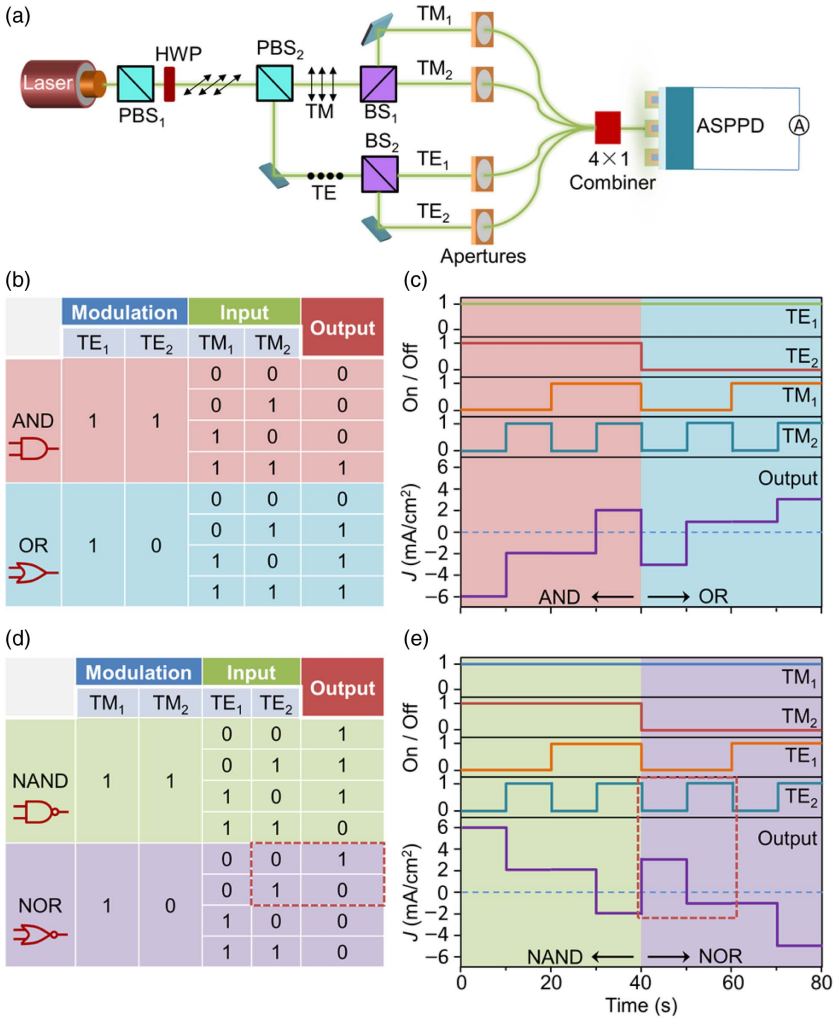

Fig. 4. (a) Full-functional PELG system. (b), (d) Truth tables of different logic functions. (c), (e) Corresponding electrical output responses for different logic configurations. Note that the red dotted boxes in patterns (d) and (e) display, respectively, the truth table and electrical output of the NOT gate.

defined as TM_1, TM_2, TE_1, and TE_2. Each beam passes through an aperture to control the on–off status. After that, one beam is synthesized through a 4 × 1 combiner to illuminate the ASPPD. The photocurrent of the PD is shown by the ammeter. In general, one or two of the four beams are taken as logically optical inputs, and the on-state of the aperture is defined as logically "true" (1) and the off-state as logically "false" (0). The response current of the PD is taken as logically electrical output, and the positive (negative) current is judged as 1 (0). The following is a description of implementing various logic functions based on a single PD without reconfiguring the PD circuit.

AND. To implement the AND function, the HWP is regulated with the intensity ratio (I_{TE}/I_{TM}) between TE and TM components of linearly polarized light of 3:4. In this case, the intensity ratio (I_{TE1}:I_{TE2}:I_{TM1}:I_{TM2}) of the four beams is 3:3:4:4. Then, TE_1 and TE_2 are set as modulation ports, the corresponding apertures are opened, and TM_1 and TM_2 are set as two logically optical input ports. When the input logic is 00, 01, or 10, which means at most one logically optical input port is opened, the output logic is 0 since the current produced by the TM component of the light irradiated onto the ASPPD is always smaller than the TE component; when the input logic is 11, the output logic is 1, as shown in the truth table in Fig. 4(b). The corresponding output current in Fig. 4(c) also confirms the AND truth table, indicating that the AND function is implemented successfully. It should be noted that $I_{TE}/I_{TM} = 3:4$ is just an example for demonstration. It is applicable as long as $1/2 < I_{TE}/I_{TM} < 1$, considering the photocurrent anisotropy ratio is −1. This implies that the HWP modulation is robust.

OR. On the basis of the AND gate configuration, the aperture controlling TE_2 is closed, and TM_1 and TM_2 are still regarded as two logically optical inputs to perform the OR function. In this case, the response current is negative (that is, the output logic is 0) only when the input logic is 00, as shown in Figs. 4(b) and 4(c), demonstrating that the OR function is realized.

NAND. To perform the NAND function, the HWP is regulated, and I_{TE}/I_{TM} is fixed at 4:3. Here, 4:3 is again only a case for demonstration (it is valid as long as $1/2 < I_{TM}/I_{TE} < 1$). Then, the apertures controlling TM_1 and TM_2 as modulation

ports are opened, and TE_1 and TE_2 are set as two logically optical inputs. The output logic is 0 only when the input logic is 11, as shown in the mutually verified truth table and output current in Figs. 4(d) and 4(e), indicating that the NAND function is implemented.

NOR. Based on the NAND gate configuration, the aperture controlling TM_2 is closed, and TE_1 and TE_2 are still regarded as two logically optical inputs to perform the NOR function. In this case, the response current is positive only when the input logic is 00, as shown in Fig. 4(e), indicating the NOR function is realized.

NOT. On the basis of the NOR gate configuration, TE_1 is also set as a modulation port with a closed aperture, and only TE_2 is regarded as one logically optical input to perform the NOT function. The red dotted box in Fig. 4(d) displays the truth table of the NOT gate. In this case, the logical value of the electrical output is opposite to that of the optical input, as shown in the red dotted box in Fig. 4(e), demonstrating that the NOT function is implemented.

So far, all five basic logic functions have been realized based on a single ASPPD. As we know, the NOR gate has functional completeness, so more comprehensive logic functions can be further achieved based on the device. The proposed PELG is based on the split polarized beams of a single light source, so the power disturbance of the light source will not affect the logic operation, and the whole PELG can operate at lower power consumption. As shown in Fig. 3(a), $J_{TM}/J_{TE} = -1$ can be maintained in a wide range of incident powers. More generally, if $J_{TM}/J_{TE} = -k$ $(k > 0)$ at other structure sizes and/or wavelengths, various logic functions can still be achieved by modulating HWP only if I_{TE}/I_{TM} is from $0.5k$ to k when performing AND and OR logic, and from k to $2k$ for NAND, NOR, and NOT logic. In general, the proposed PELG shows strong robustness against structure size, incident wavelength, light power, and HWP modulation. It should be noted that the optical system here is only a demonstration, and multiple optical logic elements can be further integrated on a chip for future practical applications [34,35]. In addition, if the material quality is poor in practical preparation, the photoelectric response performance of the device will deteriorate. For example, a smaller difference of electron and hole mobilities will lead to a smaller response current and responsivity, and a larger recombination rate will also lead to a smaller response current and responsivity [36,37]. These factors will eventually lead to poor robustness of the PELG.

3. CONCLUSIONS

In summary, we proposed an ASPPD based on a nested grating to realize an all-in one PELG. By controlling the optical field distribution in the nanostructure-based Dember device utilizing optical resonance modes (i.e., WGM and LSP), the PD at zero bias achieves ambipolar photocurrents under TE and TM incidences. Further, a full-functional PELG composed of one light source and one PD only is proposed utilizing the current ambipolarity modulated by light polarization. A linearly polarized beam is decomposed into two TM beams and two TE beams. Taking two or one of the four beams as logically optical inputs and the response current of the ASPPD as logically electrical output, all five basic logic functions (i.e., AND, OR, NOT, NAND, and NOR) are realized without reconfiguring the PD circuit. It is also found that the PELG shows a strong robustness against structure size ($20\ \text{nm} < d_{Ag} < 110\ \text{nm}$ and $70\ \text{nm} < d_{MAPbI3} < 110\ \text{nm}$), wavelength ($400\ \text{nm} \le \lambda \le 570\ \text{nm}$), light power ($10^{-4}$ – $10^{2}\ \text{W/m}^2$), and HWP modulation. The ultra-short response time (131 ns) of the PD indicates that the logic gate has a high bandwidth. Therefore, the all-in-one scheme promotes the development of PELGs towards high integration, high precision, low power consumption, high bandwidth, and multi-functionalities.

Funding. National Key Research and Development Program of China (2022YFB4200901); National Natural Science Foundation of China (62105126, 62120106001, 62005188); Natural Science Foundation of Jiangsu Province (BK20210454); Priority Academic Program Development of Jiangsu Higher Education Institutions.

Acknowledgment. We acknowledge Prof. Jingpei Hu of Shanghai Institute of Optics and Fine Mechanics, Chinese Academy of Sciences, for guidance in polarization detection. We acknowledge Prof. Zhihao Bian of Jiangnan University for guidance in the optical system.

Disclosures. The authors declare no competing financial interests.

Data Availability. Data underlying the results may be obtained from the authors upon reasonable request.

REFERENCES

1. T. Boolakee, C. Heide, A. Garzón-Ramírez, H. B. Weber, I. Franco, and P. Hommelhoff, "Light-field control of real and virtual charge carriers," Nature **605**, 251–255 (2022).
2. M. Prasad and S. Roy, "Optoelectronic logic gates based on photovoltaic response of bacteriorhodopsin polymer composite thin films," IEEE Trans. NanoBiosci. **11**, 410–420 (2012).
3. Y. Liu, S. Wang, H. Liu, and L. M. Peng, "Carbon nanotube-based three-dimensional monolithic optoelectronic integrated system," Nat. Commun. **8**, 15649 (2017).
4. J. Cahoon, "Letting photons out of the gate," Nat. Nanotechnol. **12**, 938–939 (2017).
5. W. Kim, H. Kim, T. J. Yoo, J. Y. Lee, J. Y. Jo, B. H. Lee, A. A. Sasikala, G. Y. Jung, and Y. Pak, "Perovskite multifunctional logic gates via bipolar photoresponse of single photodetector," Nat. Commun. **13**, 720 (2022).
6. Y. Q. Bie, Z. M. Liao, H. Z. Zhang, G. R. Li, Y. Ye, Y. B. Zhou, J. Xu, Z. X. Qin, L. Dai, and D. P. Yu, "Self-powered, ultrafast, visible-blind UV detection and optical logical operation based on ZnO/GaN nanoscale p-n junctions," Adv. Mater. **23**, 649–653 (2011).
7. X. Wang, Y. Zhang, X. Chen, M. He, C. Liu, Y. Yin, X. Zou, and S. Li, "Ultrafast, superhigh gain visible-blind UV detector and optical logic gates based on nonpolar a-axial GaN nanowire," Nanoscale **6**, 12009–12017 (2014).
8. B. J. Kim, N. K. Cho, S. Park, S. Jeong, D. Jeon, Y. Kang, T. Kim, Y. S. Kim, I. K. Han, and S. J. Kang, "Highly transparent phototransistor based on quantum-dots and ZnO bilayers for optical logic gate operation in visible-light," RSC Adv. **10**, 16404–16414 (2020).
9. M. Li, J. Xu, K. Zhu, S. Shi, Q. Zhang, Y. Bu, J. Chen, J. Xu, Q. Zheng, Y. Su, X. Zhang, and L. Li, "The fabrication of a self-powered $CuInS_2$/TiO_2 heterojunction photodetector and its application in visible light

communication with ultraviolet light encryption," J. Mater. Chem. C **9**, 14613–14622 (2021).
10. L. Ding, N. Liu, L. Li, X. Wei, X. Zhang, J. Su, J. Rao, C. Yang, W. Li, J. Wang, H. Gu, and Y. Gao, "Graphene-skeleton heat-coordinated and nanoamorphous-surface-state controlled pseudo-negative-photoconductivity of tiny SnO_2 nanoparticles," Adv. Mater. **27**, 3525–3532 (2015).
11. A. Rogalski, *Infrared Detectors* (CRC Press, 2010).
12. G. Cao, Y. An, Q. Bao, and X. Li, "Physics and optoelectronic simulation of photodetectors based on 2D materials," Adv. Opt. Mater. **7**, 1900410 (2019).
13. G. Cao, H. Zhang, G. Chen, and X. Li, "Ambipolar self-driving polarized photodetection," ACS Photon. **8**, 2459–2465 (2021).
14. G. Cao, H. Zhang, C. Wang, and X. Li, "Self-driving perovskite Dember photodetectors," Adv. Opt. Mater. **10**, 2101821 (2022).
15. X. Li, N. P. Hylton, V. Giannini, K. H. Lee, N. J. Ekins-Daukes, and S. A. Maier, "Multi-dimensional modeling of solar cells with electromagnetic and carrier transport calculations," Prog. Photovolt. Res. Appl. **21**, 109–120 (2013).
16. X. Li, N. P. Hylton, V. Giannini, K. H. Lee, N. J. Ekins-Daukes, and S. A. Maier, "Bridging electromagnetic and carrier transport calculations for three-dimensional modeling of plasmonic solar cells," Opt. Express **19**, A888–A896 (2011).
17. M. I. Saidaminov, A. L. Abdelhady, B. Murali, E. Alarousu, V. M. Burlakov, W. Peng, I. Dursun, L. Wang, Y. He, G. Maculan, A. Goriely, T. Wu, O. F. Mohammed, and O. M. Bakr, "High-quality bulk hybrid perovskite single crystals within minutes by inverse temperature crystallization," Nat. Commun. **6**, 7586 (2015).
18. G. H. Meng, Y. P. Feng, X. D. Song, Y. T. Shi, M. Ji, Y. Xue, and C. Hao, "Theoretical insight into the carrier mobility anisotropy of organic-inorganic perovskite $CH_3NH_3PbI_3$," J. Electroanal. Chem. **810**, 11–17 (2018).
19. W. Tian, C. Zhao, J. Leng, R. Cui, and S. Jin, "Visualizing carrier diffusion in individual single-crystal organolead halide perovskite nanowires and nanoplates," J. Am. Chem. Soc. **137**, 12458–12461 (2015).
20. H. Yu, J. Ryu, J. W. Lee, J. Roh, K. Lee, J. Yun, J. Lee, Y. K. Kim, D. Hwang, J. Kang, S. K. Kim, and J. Jang, "Large grain-based hole-blocking layer-free planar-type perovskite solar cell with best efficiency of 18.20%," ACS Appl. Mater. Interfaces **9**, 8113–8120 (2017).
21. M. Hirasawa, T. Ishihara, T. Goto, K. Uchida, and N. Miura, "Magnetoabsorption of the lowest exciton in perovskite-type compound (CH_3NH_3) PbI_3," Physica B **201**, 427–430 (1994).
22. G. Giorgi, J. I. Fujisawa, H. Segawa, and K. Yamashita, "Small photocarrier effective masses featuring ambipolar transport in methylammonium lead iodide perovskite: a density functional analysis," J. Phys. Chem. Lett. **4**, 4213–4216 (2013).
23. H. J. Snaith, M. B. Johnston, R. L. Milot, G. E. Eperon, and L. M. Herz, "Temperature-dependent charge-carrier dynamics in $CH_3NH_3PbI_3$ perovskite thin films," Adv. Funct. Mater. **25**, 6218–6227 (2015).
24. C. Czekalla, T. Nobis, A. Rahm, B. Cao, J. Zúñiga-Pérez, C. Sturm, R. Schmidt-Grund, M. Lorenz, and M. Grundmann, "Whispering gallery modes in zinc oxide micro- and nanowires," Phys. Status Solidi B **247**, 1282–1293 (2010).
25. L. Huang, Y. Yu, and L. Cao, "General modal properties of optical resonances in subwavelength nonspherical dielectric structures," Nano Lett. **13**, 3559–3565 (2013).
26. R. S. Moirangthem, P. J. Cheng, P. C. H. Chien, B. T. H. Ngo, S. W. Chang, C. H. Tien, and Y. C. Chang, "Optical cavity modes of a single crystalline zinc oxide microsphere," Opt. Express **21**, 3010–3020 (2013).
27. C. Zou, C. Dong, J. Cui, F. Sun, Y. Yang, X. Wu, Z. Han, and G. Guo, "Whispering gallery mode optical microresonators: fundamentals and applications," Sci. China-Phys. Mech. Astron. **42**, 1155–1175 (2012).
28. Z. Wang and B. Nabet, "Nanowire optoelectronics," Nanophotonics **4**, 491–502 (2015).
29. Muhammad, C. Lim, J. Reddy, E. Carrera, X. Xu, and Z. Zhou, "Surface elastic waves whispering gallery modes based subwavelength tunable waveguide and cavity modes of the phononic crystals," Mech. Adv. Mater. Struc. **27**, 1053–1064 (2020).
30. M. Dąbrowski, Y. Dai, A. Argondizzo, Q. Zou, X. Cui, and H. Petek, "Multiphoton photoemission microscopy of high-order plasmonic resonances at the Ag/Vacuum and Ag/Si interfaces of epitaxial silver nanowires," ACS Photon. **3**, 1704–1713 (2016).
31. K. Guo, M. Li, X. Fang, X. Liu, Y. Zhu, Z. Hu, and X. Zhao, "Enhancement of properties of dye-sensitized solar cells by surface plasmon resonance of Ag nanowire core–shell structure in TiO_2 films," J. Mater. Chem. A **1**, 7229–7234 (2013).
32. S. Bae, H. Han, J. G. Bae, E. Y. Lee, S. H. Im, D. H. Kim, and T. S. Seo, "Growth of silver nanowires from controlled silver chloride seeds and their application for fluorescence enhancement based on localized surface plasmon resonance," Small **13**, 1603392 (2017).
33. H. Eom, J. Jung, Y. Shin, S. Kim, J. Choi, E. Lee, J. Jeong, and I. Park, "Strong localized surface plasmon resonance effects of Ag/TiO_2 core-shell nanowire arrays in UV and visible light for photocatalytic activity," Nanoscale **6**, 226–234 (2014).
34. D. Jevtics, J. A. Smith, J. McPhillimy, B. Guilhabert, P. Hill, C. Klitis, A. Hurtado, M. Sorel, H. H. Tan, C. Jagadish, M. D. Dawson, and M. J. Strain, "Spatially dense integration of micron-scale devices from multiple materials on a single chip via transfer-printing," Opt. Mater. Express **11**, 3567–3576 (2021).
35. M. R. Fetterman, "Design for high-speed optoelectronic Boolean logic," IEEE Photon. Technol. Lett. **21**, 1740–1742 (2009).
36. Y. Wan, C. Shang, J. Huang, Z. Xie, A. Jain, J. Norman, B. Chen, A. C. Gossard, and J. E. Bowers, "Low dark current 1.55 Micrometer InAs quantum dash waveguide photodiodes," ACS Nano **14**, 3519–3527 (2020).
37. B. Chen, Y. Wan, Z. Xie, J. Huang, N. Zhang, C. Shang, J. Norman, Q. Li, Y. Tong, K. M. Lau, A. C. Gossard, and J. E. Bowers, "Low dark current high gain InAs quantum dot avalanche photodiodes monolithically grown on Si," ACS Photon. **7**, 528–533 (2020).